

## A PERFORMANCE AND APPLICATIONS STUDY OF THE PHOTOELECTRON SPECTROMICROSCOPE\*

MICHAEL KEENLYSIDE  
257 Farley St., Mountain View, CA 94043

PIERO PIANETTA  
*Stanford Linear Accelerator Center, Stanford Synchrotron Radiation Laboratory  
Stanford University, Stanford, CA 94309, U.S.A.*

### ABSTRACT

We review some recent work carried out in the area of Photoelectron Spectromicroscopy for both laboratory and synchrotron based instruments. This allows assessment of the technique's capability for dealing with real world applications. In particular, a comparison of achieved performance is made with commercial laboratory equipment to illustrate the strength of the technique. Examples of applications are also given to highlight its versatility and flexibility. Finally we address some of the present limitations of the technique and make specific proposals to expand its applications role.

### INTRODUCTION

During the late 1970's a new approach to conducting micro-area photoelectron imaging and spectroscopy was explored by an Oxford University group led by D. W. Turner (1, 2). The technique, dubbed Photoelectron Spectromicroscopy (PESM) uses a high field superconducting solenoid to guide and collimate electrons which are photo-excited from a sample situated close to the magnetic center of the system. The photoelectrons are then intercepted by some detector/spectrometer combination which is positioned on the solenoid axis (Figure 1). In general all of the photoelectrons are emitted with components of momentum both parallel and transverse to the magnetic field direction. The transverse momentum component has the effect of tightly binding each emitted electron to the magnetic field lines passing through the point of emission by virtue of the gyro-magnetic force. The parallel component translates the electron toward a region of decreasing field. Both components combine to produce a helical trajectory with its guiding center aligned with the magnetic field direction. As the electrons move into a region of decreasing magnetic field, the axial and radial Lorentz forces (see inset Figure 1) cause an interchange of the electron momentum from the radial to the axial sense (the process conserving both linear and angular momentum) until finally the electron motion becomes essentially linearized or collimated with the magnetic field direction.

*Submitted to the Journal of Electron Spectroscopy and Related Phenomena.*

---

\* Work Supported by the U.S. Department of Energy under Contract DE-AC03-76SF00515

As the diverging magnetic field lines act as guiding tracks for electrons emitted over the sample, registration between neighboring electrons is maintained and the sample information is mapped out into the lower field region preserving spatial integrity ( within several cyclotron radii) and giving subsequent magnification. This projection optics possesses the unique capability of capturing the total emitted electron flux irrespective of initial take-off angle and so provides the ultimate in collection efficiency. At some suitable on-axis location an entrance aperture may be inserted into the drift path of the photoelectrons and imaging or spectral analysis can be carried out of some selected sample area of interest.

Several different analysis schemes have been employed to detect the spectrum of incoming electrons (3, 4, 5) the easiest method employs a retarding potential analyzer. In this case, assuming the magnetic field ratio  $B(\text{sample})/B(\text{detector})$  is sufficiently high, the residual transverse component of the electron momentum at the analysis plane represents only a very small fraction of the total momentum and theoretically, at least, it can be ignored in an energy analysis.

Up until the present time, most of the samples analyzed in the literature using this technique have been conducting or semiconducting in nature. However, there are many other important potential applications which require the analysis of insulators. Examples range over glass and carbon fiber composites, catalysts, plastic and paint films, cloth, rubber and paper. Typical samples usually have poor photoemission yields, may be rough in topography or even particulate in form in addition to having surface chemistry which displays only subtle spectral line shifts. Here our objective is to illustrate the versatility of Photoelectron spectromicroscopy, in both a synchrotron and laboratory context and then assess its capability as an applications tool for general surface studies.

## EXPERIMENTAL ARRANGEMENT

The essential instrumentation common to all of the experimental work described here is shown in Figure 2. The vacuum system base pressure is typically operated in the UHV region ( $< 1 \times 10^{-8}$  Torr) and the collimation path from sample to the detector/spectrometer is approximately 1.5 meters. The superconducting solenoid is contained within a liquid helium cooled dewar which is demountable from the vacuum chamber. The magnetic field strengths at the sample and analysis planes (i.e., the entrance aperture to the energy analyzer) are typically 7 Tesla and 0.003 Tesla, respectively. At the detector plane, the magnetic field is 0.0015 Tesla.

Several experimental configurations have been studied. These variations relate to two key areas: 1) differences in the imaging and spectroscopy philosophies; and 2) differences in the excitation sources.

### Imaging and Spectroscopy

Different versions of electron spectrometer and image detector design combinations are discussed here. They are:

a) A retarding potential analyzer with a 2-dimensional microchannel plate (MCP)/resistive anode pulse position detector (6). This analyzer records each incoming photoelectron event in addition to its arrival location on the detector input plane. All such events are subsequently stored in a two dimensional array within an HP 300 workstation. The spatial distribution of the photoelectrons in any spectral band can then

be obtained by collecting images at both band extremes and then carrying out image differencing within the computer(5).

b) A trochoidal analyzer, with pre-retardation elements and a series of selectable entrance apertures, located on-axis in the low field region of the superconducting solenoid. In this arrangement an MCP/phosphor screen direct image detector was mounted on axis and in the exit plane of the trochoidal analyzer. To obtain direct photoelectron images the trochoidal analyzer was switched off and a series of axial gates through the spectrometer were simultaneously opened to permit passage of the electrons composing the image.

c) A conventional hemispherical energy analyzer (HSA) with preretardation elements and selectable entrance apertures. The HSA was in this case mounted outside of a magnetic field termination such that the energy analysis and preretardation occurred within a magnetically screened volume. In this case imaging was carried out with a 2-d MCP/resistive anode pulse position detector fixed to one end of an externally adjustable vacuum rotary feed through. The detector was located upstream of the HSA and located within the magnetic field region(4).

d) An imaging band pass analyzer composed of two 90 degree spherical sectors. The energy analyzer is operated with the same type of magnetic termination as used in the HSA described above. The analyzer is arranged such that the first spherical sector focuses the parallel electron beam coming from the Photoelectron Spectromicroscope onto a slit where the energy analysis is performed. The second sector acts like projection lens, taking the electron distribution coming through the slit and forming an image of the sample on an MCP/resistive anode detector. This analyzer has been tested and has been able to maintain the spatial resolution of the Photoelectron Spectromicroscope at an energy resolution of 0.5 eV(7). This analyzer was described since it is conceptually an extension of the HSA described above but it will not be discussed further.

### Radiation Sources

The sources used to excite electron emission in the work described include a) tunable synchrotron radiation from the Stanford Synchrotron Radiation Laboratory using experimental stations with photon energies in range 10 eV to 1500 eV (8); b) Al  $K_{\alpha}$  radiation from a laboratory source (Figure 2, inset a); c) a fast atom source also used for sample surface cleaning; d) a conventional windowless ultraviolet lamp; and e) an optical light source.

## RESULTS AND DISCUSSION

In this section we evaluate the performance of the Photoelectron Spectromicroscope and show some examples which demonstrate its versatility and flexibility. Further we discuss some future enhancements which should extend the applications role of the instrument .

### Spatial Resolution

At the time of the technique's inception the spatial resolution capability was viewed by many as its principal attraction, specifically as a means of carrying out micro-area XPS. An illustration of the resolution achievable with varying photoelectron kinetic energy is shown in Figure 3 (9, 10). For tunable synchrotron sources, in particular, advantage can be taken of the resolution improvement available at low photoemission energies. This can be done by tuning the energy of the incident radiation to a value above the excitation threshold so that core levels of interest can be excited with minimum kinetic energy. The example that will be used to illustrate this approach was carried out at SSRL in which a sample consisting of a 25  $\mu\text{m}$  aluminum line and an aluminum pad on a silicon substrate

was excited with monochromatic 170 eV radiation (5). Images with spectroscopic information are acquired using a retarding potential analyzer in which a series of images are taken at different values of retarding potential. In this case, nineteen images were taken at different retarding fields from 85.5 to 94.5 volts, 0.5 volts apart. An analysis of the raw images indicated that the Al 2p electrons coming from the pad had a binding energy of 91.25 eV while those coming from the line had a binding energy of 90.25 eV. The effect of this shift on the images is shown in Figure 4. Figure 4a shows a differential image obtained by subtracting the image taken at a retarding field of 93.5 volts from the image taken at 90.5 volts. The high intensity regions are clustered mostly on the aluminum pad and emphasize the surface features associated with the 91.25 volt binding energy peak. Figure 4b shows a differential image obtained by subtracting the image taken at a retarding field of 90.5 volts from the image taken at 85.5 volts. In this case, the contribution from the pad is removed and the area associated with the 90.25 volt binding energy peak (the aluminum line) is enhanced. The intensity on the far right of this image is an artifact due to spatial non-uniformity in the photon beam and can be removed when the images are normalized before subtraction.

Further enhancement to the spatial resolution should be possible (at the expense of total collection efficiency) using an angular selection scheme to allow transmission of only trajectories having reduced cyclotron radii. This "skimming" principle is described in Figure 5. Electrons leaving the sample pass through a retarding electrostatic field arranged near the system center in a region of uniform magnetic field. The retarding potential ideally acts only on the parallel component of electron momentum  $p_{//}$ . Transmission through the skimming retarding field occurs for electrons with total linear momentum  $p_{//}$  when:

$$p_{//}^2 \geq 2meV_s \quad \text{where, } V_s \text{ is the skimming voltage;}$$

or in energy terms, when:

$$E \cos^2 \theta_s \geq eV_s$$

where  $\theta_s = \cos^{-1}(p_{//}/p)$  is the angle between the total linear momentum vector,  $p$ , and the solenoid axis and  $E$  is the electron kinetic energy. Cut-off then occurs when

$$E \cos^2 \theta_s = eV_s$$

leading to

$$\sin^2 \theta_s = (1 - eV_s/E)$$

For the collimation process  $p_{\perp}^2/B$  is invariant and so  $[p \sin \theta]^2/B$  is also invariant. Where  $B$  is the local magnetic field strength and  $p_{\perp}$  is the transverse component of electron momentum and  $\theta$  is the angle between the electron trajectory and the solenoid axis. As a result, at the detector, (indicated by the subscript "d"):

$$\sin^2 \theta_d = (B_d/B_s) \sin^2 \theta_s$$

The cyclotron radius at the detector/spectrometer ( $r_d$ ) is given by:

$$r_d^2 = 2mE \sin^2 \theta_d / B_d^2 e^2$$

Substituting for  $\sin^2 \theta_d$  gives:

$$r_d^2 = 2mE \sin^2 \theta_s / B_d B_s e^2$$

Hence at cut-off

$$(r_d)^2 = 2mE(1 - eV_s/E) / B_d B_s e^2$$

With E in electron volts:

$$r_d = [2mE(1 - V_s/E) / B_d B_s e]^2$$

In the case where  $V_s/E \rightarrow 0$

$$r_d \rightarrow r_{d,0} = [2mE / B_d B_s e]^2$$

So can alternatively write:

$$r_d = r_{d,0}(1 - V_s/E)^2$$

where,  $\sin \theta_s = (1 - V_s/E)^2$

Or referenced to the sample:

$$r_d = r_o(1 - V_s/E)^2 \text{ where } r_o \text{ is the cyclotron radius at the sample.}$$

The enhancement achievable in solenoid central fields of 7T is illustrated by the dashed line in Figure 3 (10). This predicted performance for electron kinetic energies of 10 eV compares favorably with that already achieved with other techniques (11, 12, 13, 14). Assuming the angular asymmetry parameter for photoemission from the sample follows a  $\cos \theta$  dependence then we estimate that a tenfold improvement in spatial resolution leads approximately to a near proportional reduction in photo-flux from an equivalent area.

### Energy Resolution

PESM X-ray excited photoemission spectra of metal standards have been shown in the literature (4). The data of Knapp et al. on silver allows measurement of the energy resolution performance at typical ESCA kinetic energies. The first three columns of Table 1 summarize these results at the smallest area analyzed.

The measured spectral line width,  $\Gamma$ , is simply the root mean square summation of each of the non-correlated contributions from source, sample and spectrometer, i.e.,

$$\Gamma^2(\text{measured}) = \Gamma^2(\text{source}) + \Gamma^2(\text{sample}) + \Gamma^2(\text{spectrometer})$$

In this case the spectrometer broadening includes both contributions from the magnetic decoupling process and the HSA. Using the known values for the natural line width of silver [0.34 eV (15)] and the source bandwidth (0.85 eV), the total spectrometer broadening and the resulting energy resolution  $KE/\Delta E$  can be found. These values are given in the last two columns of Table 1.

For a momentum analyzer, the limit in spectral resolution is given by the residual transverse momentum measured at the analysis plane. At a maximum, this contribution would be  $KE/\Delta E = B(\text{solenoid})/B(\text{detector}) = 2700$  measured at full line width as opposed to FWHM as with the above experimental data. However, it should also be noted that this calculated value excludes any inherent spectrometer contribution which is clearly unrealistic. This form of analyzer would therefore be expected to produce significantly lower resolution than this idealized value.

### System sensitivity

According to theoretical considerations one major advantage of this technique over more conventional electron lens systems is its unique collection efficiency. Some appreciation of the practical performance levels attainable and how sensitivity compares with other XPS laboratory equipment is desirable. Here to assist this process we compare data taken on a Fisons Instruments commercial S-probe system with the spectral data of Knapp et al. (4). The S-probe operates in this case with a non monochromatic X-ray source. This instrument is chosen to simplify the comparison as the HSA detection and counting electronics used in this model are almost identical to those used in the work of Knapp et al. The data from each of these instruments is given in Table 2, which shows the original measurements and the values normalized for source power and area.

Some qualifying statements are necessary in conjunction with Table 2:

- 1) The S-Probe count rate is significantly understated because the electron detector is close to saturation. It is estimated that the true count rate is a factor of two or even three times greater than indicated.
- 2) Knapp et al. data is taken on contaminated silver and the estimated improvement in this case is MK.
- 3) The PESM data is taken at an X-ray anode to sample spacing of approximately 18 mm. In the case of the S-probe system the spacing quoted is actually for sample to X-ray window (10 mm). It is assumed here that both sample to anode spacings are approximately the same.

## TECHNIQUE APPLICATIONS

Insulating Samples. In general, work on insulators is hampered in the Photoelectron Spectromicroscope by the lack of an effective charge control technique. Without charge stabilization spectral lines are shifted to lower kinetic energy and line broadening occurs smearing out valuable chemical information. In some cases analysis may even be prevented. The problems are similar to those experienced with monochromatic laboratory XPS systems where flood gun or alternative approaches are required (16). In contrast, for non-monochromatic laboratory systems electron replenishment to the analyzed sample occurs via secondary emissions from surrounding surfaces in the vacuum chamber. However in the PESM the confining magnetic field prohibits this

particular mechanism. Charge control using a low energy electron flood gun is also restricted to an on-axis arrangement because the solenoid acts as a magnetic mirror, reflecting all but those electrons traveling parallel to the axis. A technique used here for overcoming this problem when operating with the Al  $K_{\alpha}$  X-ray source is illustrated in Figure 2 (inset b). The data shown in Figure 6a is taken on a SiO<sub>2</sub> plate and charge stabilization was achieved with a 400 line per inch copper mesh placed approximately 10 mm in front of the sample. Figure 6b shows the result of removing the mesh.

Although the back illumination technique described clearly stabilizes the sample surface it does have certain drawbacks:

- a) The grid partially obscures the field of view of the sample and consequently reduces signal intensity.
- b) Photoelectrons emitted from the edges of the grid are detected at the analyzer and so contribute to the spectrum.
- c) Charge broadening still occurs since the electrons emitted in the direction of the sample have a nonuniform spatial distribution which in turn leads to differential charging.

An improved charge compensation scheme we are proposing to overcome this problem is given in Figure 7. In essence the copper grid previously described is here replaced with a sheath of inert gas at a variable pressure estimated to be in the range  $1 \times 10^{-2}$  to  $1 \times 10^{-5}$  Torr. The gas is illuminated with vacuum UV radiation to excite low energy electron emission immediately in front of the sample. A uniform flux of low energy electrons is then available to replenish any negative charge lost by photoemission. Two important considerations of such a system are:

- 1) The electron mean free path: photoemitted electrons must pass through the high pressure zone without interaction. The mean free path at a pressure of  $1 \times 10^{-2}$  Torr is estimated from gas dynamics (17) as being approximately 1.5 cm.
- 2) The total photoelectron ionization cross section: This has to be sufficiently large in order to generate a supply of neutralizing electrons to replenish the sample. For a conventional capillary HeI discharge lamp giving a flux of  $1 \times 10^{10}$  photons/sec into an argon gas pressure of  $1 \times 10^{-2}$  Torr the electron yield is estimated to be:

$$Y = n_p \sigma N x$$

where  $n$  is the number of primary photons,  $\sigma$  is the Ar 3p interaction cross section (38 MB/atom) (18),  $N$  is the number of atoms/unit volume ( $3.9 \times 10^{20}$ ), and  $x$  is the length of ionized volume (1 cm). This gives  $Y = 1.5 \times 10^8$  electrons/sec. This result is a factor of 10 less than the values determined experimentally (19) which indicates that the yield is indeed a factor of 10 greater than what is estimated in the calculation, probably resulting from an underestimation here of the UV lamp photon flux.

From experimental data, we can estimate the magnitude of the X-ray photon flux which the technique should sustain, assuming the sample electrically floats, by considering the sample quantum efficiency, i.e., the number of electrons ejected from the sample surface per incident photon (20). Taking gold which has a rather high quantum efficiency, 0.055 electrons/photon, as an example, an incident flux as high as  $2.7 \times 10^9$  photons/sec at the energy of the Al  $K_{\alpha}$  spectral line could be used within a sample area approximately 1 mm in diameter. In contrast, carbon has a quantum efficiency which is approximately two orders of magnitude less than gold and so should be capable of operating at a proportionately higher photon flux. As the quantum efficiency is strongly sensitive to photon absorption in the surface layers, we may expect many insulators to be well suited

to this charge compensation scheme and operation at photon fluxes well in excess of  $1 \times 10^{10}$  photons/mm<sup>2</sup> should be achievable.

Irregular Samples (Particle Analysis). Figure 8 shows an image taken from a selection of semiconductor particles during light sputter etching, i.e., in this case electrons excited by the fast atom source that are sputtering the sample are being used to image the samples as well. Subsequent to the etching process, the aluminum x-ray source was switched on and the areas shown have been sequentially analyzed using a trochoidal analyzer as shown in Figure 9. This example highlights one of the important features of the technique which is the very high instrument depth of field. In this case the sample stage has simply been translated normally to the magnetic axis to analyze each of the regions identified in the image. No attempt was made, nor indeed was necessary, to re-align the sample axial position between spectra in order to correct for particle dimensional differences.

Photoabsorption Measurements. In addition to core level photoelectron spectroscopy, the ability to perform Surface Extended X-ray Absorption Fine Structure (SEXAFS) or X-ray Absorption Near Edge Structure (XANES also called NEXAFS) (21, 22) over micron sized areas could have important applications to a large number of fields. Such spectra are obtained by measuring all of the electrons that are emitted from a surface as a function of photon energy across an absorption edge of interest. Not surprisingly, this is known as total yield detection. In this way, it is possible to determine the composition of a surface down to better than 1% of a monolayer using XANES, i.e., the absorption edge information, and even the local atomic structure around a particular species using the EXAFS, i.e., the oscillations in the absorption coefficient >20 eV above the absorption edge. In performing such an analysis, the sample is first imaged and the area of interest is brought into the field of view. An aperture is then brought in front of the detector to occlude all but the area of interest. The electrons incident on the sample represent only those electrons coming from the area of interest and are detected using either the imaging detector, which is useful for insuring that small features remain in the field of view, or a high current channeltron for high counting rate applications. In this way, it has been possible to analyze structures as small as 20  $\mu\text{m}$  surrounded by an unknown matrix.

An example which demonstrates this capability is an analysis of a possible residue at the bottom of a 50  $\mu\text{m}$  square hole etched in a 1  $\mu\text{m}$  thick photoresist (23, 24). In this case, it was of interest to determine if the resist had been completely removed from the bottom of the hole during the development process. By measuring the XANES from within the hole using an aperture in front of the detector that allowed a 40  $\mu\text{m}$  area of the sample to be isolated for analysis, it was possible to show that there was a carbon residue inside the hole which had the identical spectral features as the resist which surrounded the hole. The XANES for the residue and the resist outside the hole are shown in Figure 10. This clearly shows that there is resist residue still present in the hole. This experiment was performed on experimental station 8-2 at SSRL which consists of a spherical grating monochromator on a bending magnet source. As a result of improvements in both the beam line and detection scheme, it should now be possible to analyze areas down to 10  $\mu\text{m}$  in diameter. As will be discussed below, 10  $\mu\text{m}$  is the physical limit in spatial resolution when total yield detection is used.

The resolution of the total yield technique is fully determined by effect of the energy distribution curve of the emitted electrons on the radius of gyration of the emitted electrons. As discussed above, the high energy electrons in the distribution that are emitted normal to the magnetic field, will have the largest radii when they impinge upon the detector or, in this case, go through the aperture in front of the detector. However, if one looks at the energy distribution coming from a sample as shown in the inset of Figure



11, it is clear that the low energy electrons that come from the low energy scattered tail contribute most to the detected signal. In fact, it is the low energy electrons that give most of the spectral information when total yield detection is used. However, high energy electrons do contribute and degrade the spatial resolution. Figure 11 attempts to estimate the spatial resolution for this apertured total yield detection mode for different energy distributions. These distributions are modeled in a worst case sense by assuming that the distribution is made up of two components. A low energy part which consists of a secondary tail that follows the "universal curve" described by Henke, Smith and Atwood (25) and assumes a work function of 3.7 eV and a high energy component which is a peak at the highest kinetic energy of interest (inset Figure 11). By then defining the lateral resolution as the diameter of the area on the surface from which 90% of the emitted electrons can travel through the defining aperture in front of the detector, it is possible to obtain the estimate shown in Figure 11. In this figure, we plot the lateral resolution on the x-axis for a given ratio of low energy to high energy electrons. In the most conservative case where we assume that the low and high energy electrons are equal, i.e., 50%, the lateral resolution is 10  $\mu\text{m}$  whereas when the low energy electrons are 100% of the total yield, the resolution is down to 2  $\mu\text{m}$ .

With the addition of a band pass analyzer to the instrument, it will be possible to accept the contribution from only a small band of electrons at low energy. In this case the resolution will be independent of the details of the energy distribution and thus set by the kinetic energy of the electrons and be determined by Figure 3. This could then give an spatial resolution of 1  $\mu\text{m}$  or better if skimming were used.

Dispenser cathode study. In another study demonstrating the versatility of the PESM, we show how spectroscopic and physical information can be linked by imaging a sample with different photon sources which look at different properties of the sample. The example we will use to illustrate this point is a study of dispenser cathodes carried out at SSRL (19). Dispenser cathodes are high efficiency electron emitters used in high power tubes such as traveling wave tubes. These cathodes are made up of a porous tungsten filled with a mixture which includes BaO. When the cathode is heated, Ba covers the surface and lowers the work function of the cathode which gives enhanced electron emission properties. The Ba covered surface has a mean work function of 2.15 eV which is low enough that photoemission can actually be achieved with visible light. The low work function is maintained even after the cathode is cooled to room temperature and until the surface is contaminated with residual chamber gases. In some cases, it is even possible to find areas on the surface that can be excited with HeNe radiation at an energy of 1.96 eV which is consistent with the observed work function variation of the dispenser cathodes of 0.2 eV.

As a result, it was possible to prepare a low work function surface by heating, cool it down and then image the surface by illuminating it with visible light. The strong magnetic field of the PESM made it possible to image the low energy electrons emitted in this way. In so doing, the low work function areas will emit electrons and appear bright on the image while high work function areas will appear dark. An example of such an image is shown in Figure 12 (19). This image shows a dark region of high work function surrounded by a bright area. The advantage of the PESM is that once the work function information has been obtained, it is possible to switch on a high energy excitation source and determine the chemical composition and state of the various areas on the image. Spectra obtained by exciting the sample with 120 eV radiation and performing a selected area retarding field analysis are shown in Figure 13. The spectra clearly show that the low work function areas are composed of tungsten and barium while the high work function areas show no tungsten and are primarily insulating barium oxide. In order to show both spectra on the same energy scale, it was necessary to shift the barium oxide

spectrum by 12 volts to compensate for the charging. This shows that the high work function region is due to inclusions of barium oxide which are known to be present in dispenser cathodes.

Again this illustrates how it is possible to use the PESM to obtain physical information, in this case work functions, and then isolate selected areas in order to perform detailed XPS analysis.

### Fermi Level Mapping.

One unique application of the PESM has been to map the band bending at the surface of a cleaved GaAs (110) single crystal (26). Extensive studies in the past 15 years have shown that there are no intrinsic surface states in the band gap of the GaAs (110) surface (27, 28, 29). As a result, a perfect GaAs (110) surface is unpinned, i.e., the position of the Fermi level in the gap of the semiconductor is determined by the bulk doping level. However, when a surface is cleaved, extrinsic states can be introduced which give a high density of states in the middle of the gap resulting in localized areas where the Fermi level is pinned at midgap. This is shown schematically in Figure 14 where the one dimensional band diagram for n-type GaAs (110) is shown for both the pinned and unpinned areas. In the unpinned region, the energy levels of the semiconductor (conduction bands, valence bands and core levels) are "flat", i.e., they all follow the Fermi level from the bulk up to the surface. In the case of the pinned areas, a high density of surface states causes the Fermi level to be pinned at midgap rather than the bulk position. As a result the bands are "bent" as they transition from the bulk to surface. Since the Fermi level is actually the reference level that is used in determining the binding energies, this has the effect of causing all the energy levels at the surface to be shifted relative to that in the bulk or an unpinned area. The length over which the energy levels relax to their bulk values is called the depletion region and is determined by the doping in the semiconductor and is typically much greater ( $> 100 \text{ \AA}$ ) than the escape depth of the electrons typically used in these experiments (about  $5 \text{ \AA}$ ). Therefore, photoemission is typically referred to as measuring the surface Fermi level position.

Since the pinning shifts all of the electronic levels rigidly, including the core levels, of the semiconductor it is possible to use the binding energy position of the Ga 3d levels in the case of GaAs to obtain an accurate map of the surface Fermi level position. Figure 15 shows the Ga 3d from pinned and unpinned regions of a sample of n-type GaAs. Note that the pinned region has a lower binding energy relative to the unpinned region. Therefore, if one uses a retarding potential analyzer set at a high enough voltage to reject most of the electrons from the unpinned Ga 3d and accept those from the pinned Ga 3d, the degree of pinning determines the strength of the signal coming from the sample. In other words, by using the PESM, the two dimensional map thus obtained will have contrast which is directly proportional to the degree of Fermi level pinning. This has been quantified and used for studies of clean and metal covered cleaved GaAs (110) surfaces (19, 26). Using this technique, it is possible to obtain Fermi level maps with a spatial resolution of  $10 \mu\text{m}$  and an energy resolution of  $0.05 \text{ eV}$ . One set of results for n-type GaAs (110) are shown in Figure 16. Figure 16a shows a  $200 \mu\text{m} \times 200 \mu\text{m}$  image with the retarding potential set at  $75.0 \text{ eV}$ . This retarding potential allows the Ga 3d levels from both the pinned and unpinned areas to reach the detector and is thus featureless except for a small round screen defect at the top of the image. Figure 16b shows an image taken with a retarding potential of  $75.8 \text{ eV}$ . This gives maximum contrast between the pinned (bright) and unpinned (dark) regions. One sees a triangularly shaped unpinned area surrounded by an area with various degrees of pinning. Using Figure 15, it is possible to calculate the contrast expected for various degrees of Fermi

level pinning. In this way, the Fermi level map shown in Figure 16c is obtained. The resolvable variation in Fermi level is 0.05 eV. One can clearly see that the triangular region is almost uniformly upinned within the 10  $\mu\text{m}$  spatial resolution of the technique and that a small rectangular region above it is not uniform but has a range of Fermi level positions in it. The large area around these two regions is completely pinned at the middle of the gap (0.7 eV below the conduction band minimum). The various features in the Fermi level map do correlate with topographic features on the surface and is another example of using the PESM to correlate the physical and electronic properties of a surface.

## CONCLUSIONS

From a performance perspective the PESM when coupled with some form of hemispherical energy analyzer clearly has a fundamental energy resolving power comparable with current laboratory instruments. In addition the high system sensitivity and spatial resolution achievable combine to provide a unique potential capability.

Synchrotron core level studies optimized for energy and spatial resolutions at low photoemission energies, together provide a very powerful surface study tool. Further, the enhanced sensitivity achievable by virtue of the source tunability and the very high collection efficiency provided by magnetic collimation reinforces the match between the synchrotron source and the technique.

For a laboratory instrument the high efficiency should also prove attractive especially if advantage can be taken of the throughput potential for large area analysis (i.e., areas  $> 1 \text{ mm} \times 1 \text{ mm}$ ). Indeed it seems that using the system as a very high throughput collection lens with the present spatial resolution capability would be very beneficial for trace element and specie distribution studies. Geometry permitting, it naturally follows that the high brightness and monochromaticity offered by a focused source of X-rays would offer additional benefits in terms of improved sensitivity and energy resolution. Moreover it would seem that a focused high brightness X-ray source is a prerequisite in order to take advantage of the PESM combination of spatial resolution and collection efficiency.

Very many XPS applications require the study of insulators and to a lesser degree irregular surface topographies, e.g., fibers or particles. These types of samples are by their very nature difficult to analyze and susceptible to deleterious surface charging effects. Assuming the charging problem can be satisfactorily overcome, then the spatial resolution and high depth of field of Photoelectron Spectromicroscopy should be applicable to a whole new range of problems in this area.

The potential to carry out high resolution imaging of core levels in the sub-micron range is a most important analytical objective. The angular selection scheme described here shows that this is, at least, possible at low photoemission energies. With synchrotron tunable sources resolutions of 1000  $\text{\AA}$  can be expected using this approach. In the case of laboratory versions of the instrument, this extended imaging capability will be restricted to a rather narrow binding energy range. None the less it is no doubt possible to use this approach to carry out submicron imaging at lower photoemission energies. For example a source of low energy photons (e.g., a He UV lamp) could be expected to attain this level of spatial performance.

Acknowledgement

One of us (PP) acknowledges support for this work from the Department of Energy, Office of Basic Energy Sciences, Division of Materials Sciences.  
References

1. G. Beamson, H. Q. Porter and D. W. Turner, *Nature* **290**, 556 (1981).
2. G. Beamson, H. Q. Porter and D. W. Turner, *J. Phys. E* **13**, 64 (1981).
3. D. W. Turner, *J. Phys. E: Sci. Instrum.* **22**, 593 (1989).
4. G. S. Knapp, M. Keenlyside and C. Griffin, *Surface and Interface Analysis* **15**, 786 (1990).
5. P. Pianetta, I. Lindau, P. L. King, M. Keenlyside, G. Knapp and R. Browning, *Rev. Sci. Instrum.* **60**, 1686 (1989).
6. C. Fermani, E. Ruiz, C. Carlson, M. Lampton and F. Paresce, *Rev. Sci. Instrum.* **53**, 570 (1982).
7. C. Kim, P. L. King, P. Pianetta, M. Kelly and C. Bryson, *Rev. Sci. Instrum.* **64**, 1187 (1993).
8. K. Cantwell and P. Pianetta, *Rev. Sci. Instrum.* **63**, 1609 (1992).
9. P. Kruit and F. H. Read, *J. Phys. E* **16**, 313 (1983).
10. P. L. King, A. Borg, C. Kim, S. A. Yoshikawa, P. Pianetta and I. Lindau, *Ultramicroscopy* **36**, 117-129 (1991).
11. P. Coxon, *J. Electron. Spectrosc.* **52**, 821 (1990).
12. H. Ade, J. Kirz, S.L. Hulbert, E.D. Johnson, E. Anderson, D Kern, *Applied Physics Letters* **19**, 1841 (1990).
13. C. Capasso, A. K. Ray-Chaudhuri, W. Ng, S. Liang, R. K. Cole, J. Wallace, F. Cerrina, G. Margaritondo, J. H. Underwood and J. Kortright, *J. Vac. Sci. Technol. A* **9**, 1248 (1991).
14. B. P. Tonner and G. R. Harp, *Rev. Sci. Instrum.* **59**, 853 (1988).
15. P. Pianetta and I. Lindau, *J. Electron Spectrosc.* **11**, 13-38 (1977).
16. C. E. Bryson, *Surface Science* **89/90**, 50 (1993).
17. A. Roth, *Vacuum Technology* (North Holland, Amsterdam, Netherlands, 1990).
18. J. J. Yeh and I. Lindau, *Atomic Data and Nuclear Data Tables* **32**, 1 (1985).
19. P. L. King, *Photoelectron Microscopy*, Thesis Stanford University (1992).
20. R. H. Day, P. Lee, E. B. Saloman and D. J. Nagel, *J. Appl. Phys.* **52**, 6965 (1981).

21. J. Haase and A. M. Bradshaw in *Synchrotron Radiation Research: Advances in Surface and Interface Science*, R. Z. Bachrach, Ed. (Plenum Press, New York, 1992), vol. 2, p. 55.
22. J. Stohr in *X-ray Absorption: Principles, Applications, Techniques of EXAFS, SEXAFS and XANES* R. Prins and D. Koningsberger, Eds. (Wiley, New York, 1985) p. 443.
23. P. L. King, A. Borg, C. Kim, P. Pianetta, I. Lindau, G. Knapp and M. Keenlyside, *Physica Scripta* **41**, 413-417 (1990).
24. P. Pianetta and P. King, in *Synchrotron Light: Applications and Related Instrumentation II* A. Craievich, Eds. (World Scientific, Singapore, 1990) pp. 28-46.
25. B. L. Henke, J. A. Smith and D. T. Attwood, *J. Appl. Phys.* **48**, 1852 (1977).
26. C. Kim, P. L. King and P. Pianetta, *J. Vac. Sci. Technol. B* **10**, 1944 (1992).
27. J. Van Laar and A. Huijser, *J. Vac. Sci. Technol.* **13**, 769 (1976).
28. W. E. Spicer, I. Lindau, P. E. Gregory, D. M. Garner, P. Pianetta and P. Chye, *J. Vac. Sci. Technol.* **13**, 780 (1976).
29. W. Gudat and D. E. Eastman, *J. Vac. Sci. Technol.* **13**, 831 (1976).

Table 1. Measured spectral line widths (FWHM) and count rates in a  $3 \times 45 \mu\text{m}^2$  field of view from Knapp et al on the Ag  $3d_{5/2}$  peak using Al  $K_{\alpha}$  x-ray source operating at 225 watts anode power. See text for further description.

Pass Energy (eV)	Count rate counts/minute	$\Gamma$ (measured) (eV)	$\Gamma$ (spectrometer) (eV)	KE/ $\Delta E$
25	8K	0.97	0.32	3500
50	10.8K	1.13	0.66	1697
100	19.3K	1.29	0.91	1230
150	23K	1.49	1.17	957

Table 2 . Count rates recorded on Silver  $3d_{5/2}$  taken with a commercial laboratory instrument compared with the spectral data taken by Knapp et al. The source is non-monochromated Al  $K_{\alpha}$  operating at 300 watts of beam power. The S-probe lens and PESM fields of view are assumed to be  $4 \times 2$  mm and  $0.16 \times 0.16$  mm<sup>2</sup>, respectively. The HSA pass energy is 150 eV in both cases.

	Measurement over actual field of view (Counts/min.)	Normalized to $1 \times 1$ mm <sup>2</sup> (Counts/min.)	Energy Resolution
S-probe <sup>†</sup>	$20 \times 10^6$	$2.5 \times 10^6$	1.8 eV
PESM	$615 \times 10^3$	$32 \times 10^6$	1.85 eV

<sup>†</sup> Courtesy of Dr. S. Westra, Fisons Instruments who also comments that state of the art performance represented by the their 220i system gives an improvement in throughput by a factor of five on that shown.

## LIST OF FIGURES

1. Principle of magnetic projection and collimation. Photoelectrons are excited from the sample and guided by the intense magnetic field of the superconducting solenoid into helical trajectories toward the detection plane. The inset shows the components of electron velocity and magnetic field which interact to guide the electrons and transfer momentum to the axial direction. These Lorentz forces are:

$$F_c = ev_{\perp} B_z \quad \text{inward binding force.}$$

$$F_z = ev_{\perp} B_r \quad \text{increases } v_z.$$

$$F_r = ev_{\parallel} B_r \quad \text{reduces } v_{\perp}.$$

2. The basic experimental arrangement used in the work described here. Inset A indicates the geometry of the Al  $K_{\alpha}$  X-ray source and sample. Inset B shows the technique used to overcome sample charging.

3. Variation of spatial resolution with photoelectron energy for a 7 Tesla central field (solid). Spatial resolution is defined as being equal to twice the cyclotron radius of electrons at the sample. Dashed line shows the spatial resolution improvement employing angular selection to 'skim off' electrons emitted with high transverse momentum.

4. Differential images emphasizing the spectral regions between (a) 91.5 and 93.5 volts; and (b) 85.5 and 90.5 volts. Field of view is 300  $\mu\text{m}$ .

5. The angular selection to (skimming) technique. A retarding electric field arranged close to the sample is used to reject photoelectrons with high transverse momentum. The electrons which overcome this barrier are then collimated in the normal way.

6. Illustrating a method of obtaining sample charge stabilization in PESM (shown in Figure 2, inset B). a) Spectrum of  $\text{SiO}_2$  plate sample; b) As previous but with grid removed.

7. Suggested improved technique for sample charge control. Inert gas is introduced into the vacuum chamber to a pressure of approximately  $1 \times 10^{-2}$  Torr in the sample vicinity. UV radiation is then used to generate low kinetic energy electrons which are attracted to a positively charged sample.

8. Selection of semiconductor particles imaged during the argon sputter cleaning process. Areas identified are: A- $\text{SiO}_2$ , B-GaAs, C-GaP, D- $\text{Si}_3\text{N}_4$ .

9. Four spectra taken sequentially from the 80  $\mu\text{m}$  regions identified in the image of Figure 8. The analysis is carried out using a source of Al  $K_{\alpha}$  x-rays and a trochoidal analyzer.

10. Carbon 1s XANES spectra taken from the bottom of a hole in a film of photoresist and from the surrounding resist. The area within the hole was selected by placing a 5 mm aperture in front of the detector which gave a 40  $\mu\text{m}$  region at the sample.



11. Estimate of the lateral resolution in small area total yield photoabsorption measurements assuming varying amounts of the total yield found in the secondary tail. The inset is an example of the energy distribution used in the calculation. In this case 90% of the yield is made up of low energy secondary electrons while the remaining 10% is distributed around 275 eV.
12. An image of an activated dispenser cathode, cooled to room temperature, excited by visible light showing a high work function inclusion.
13. Spectra taken at 120 eV from the inclusion and the surrounding matrix shown in Figure 12. The spectrum of the inclusion was shifted by +12 V to account for charging.
14. Band diagram of n-type GaAs for pinned and unpinned surfaces.
15. Representative Ga 3d core levels from pinned and unpinned surfaces excited by 100 eV photons. Electrons from a pinned region have a high kinetic energy than those from an unpinned region. With the retarding potential set to 75.8 V, more core electrons from the pinned region are allowed to pass.
16. Images and Fermi level maps obtained with the PESM and retarding field analyzer using a photon energy of 100 eV. Image size is  $200 \mu\text{m} \times 200 \mu\text{m}$ . (a) Image of a cleaved n-type GaAs (110) surface with the retarding potential set at 75.0 V; b) Same image with a 75.8 V retarding potential; c) Fermi level map in which the scale to the right of the image shows the difference in energy between the conduction band minimum and the Fermi level; d) Fermi level map of the same region covered by 0.7 monolayers of indium.

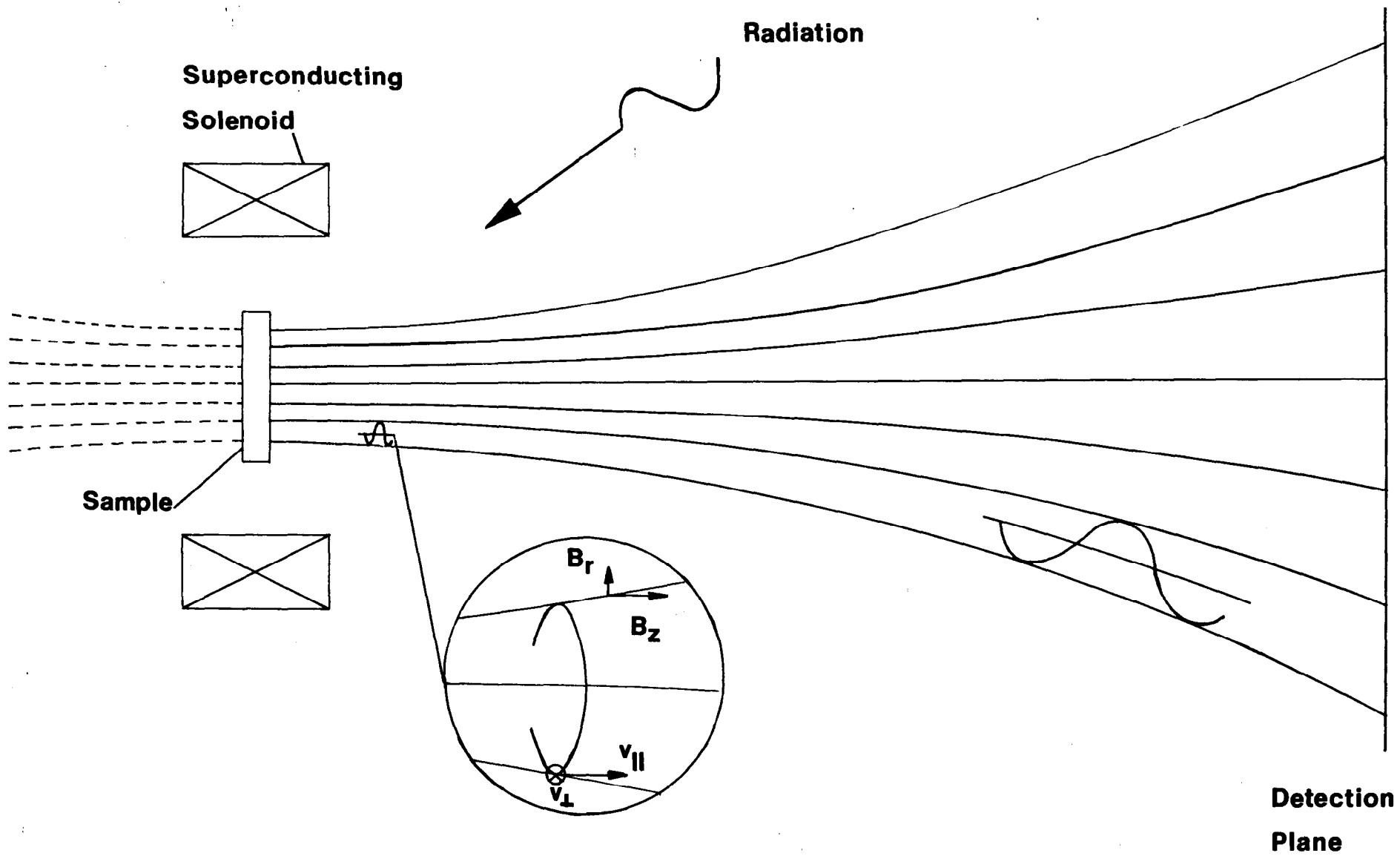


Fig. 1

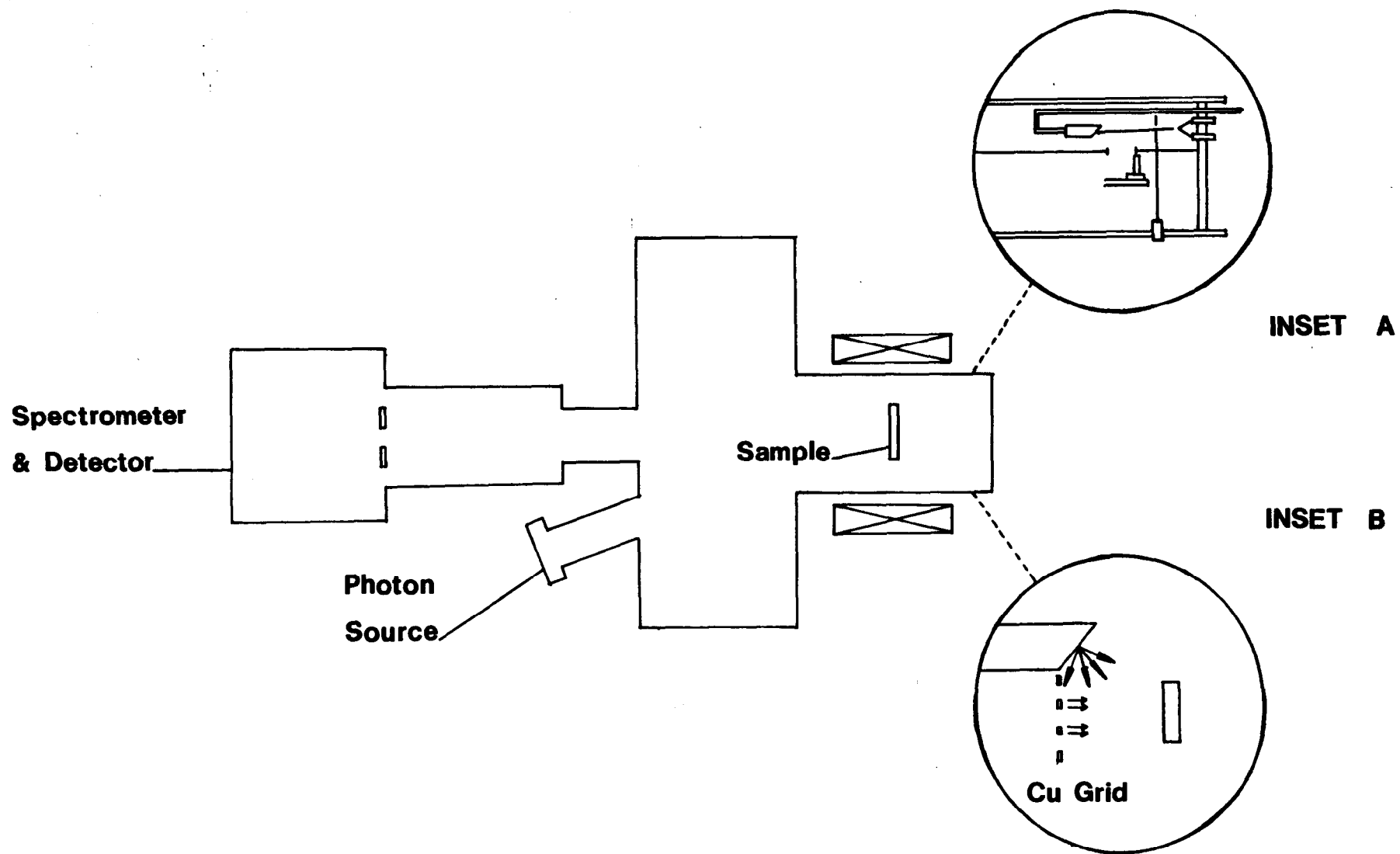


Fig. 2

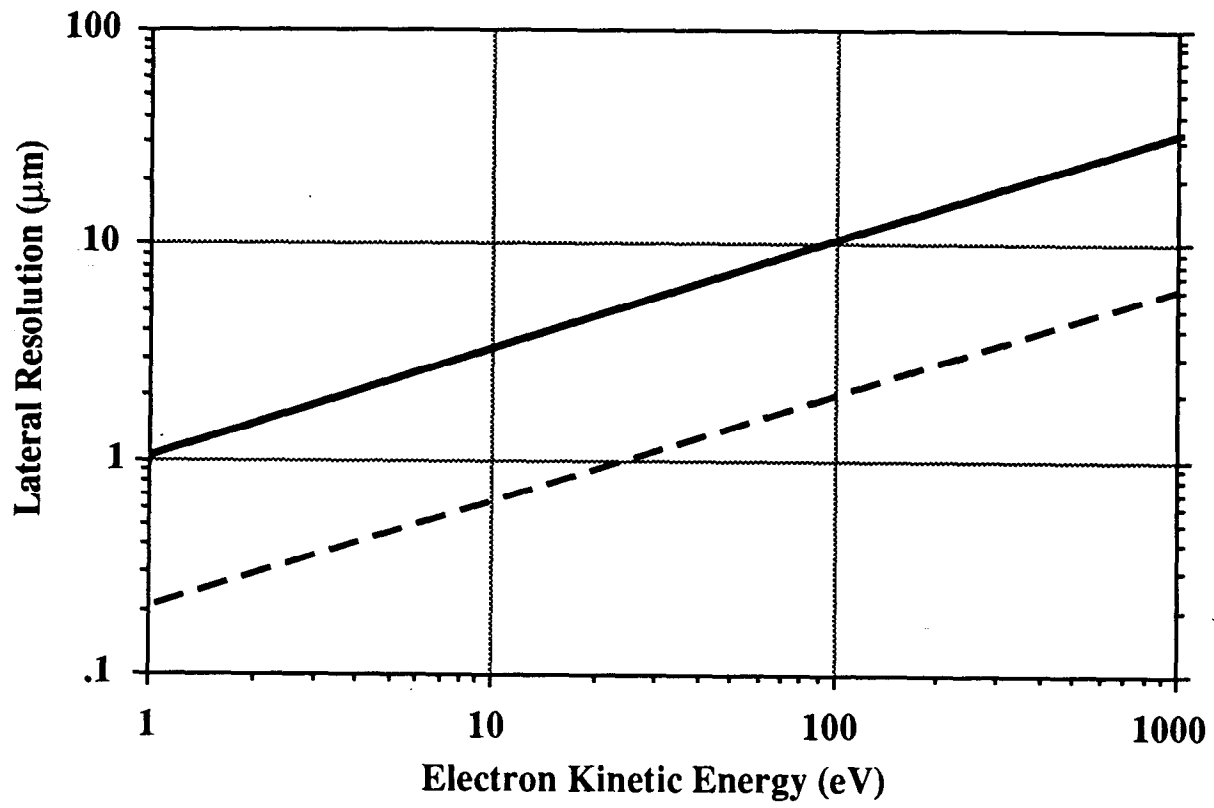


Fig. 3

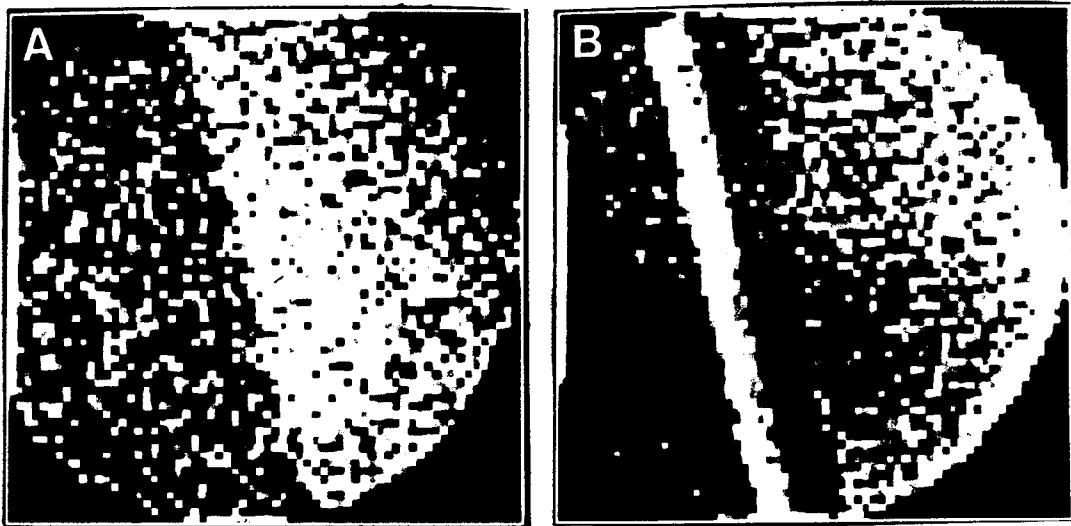


Fig. 4

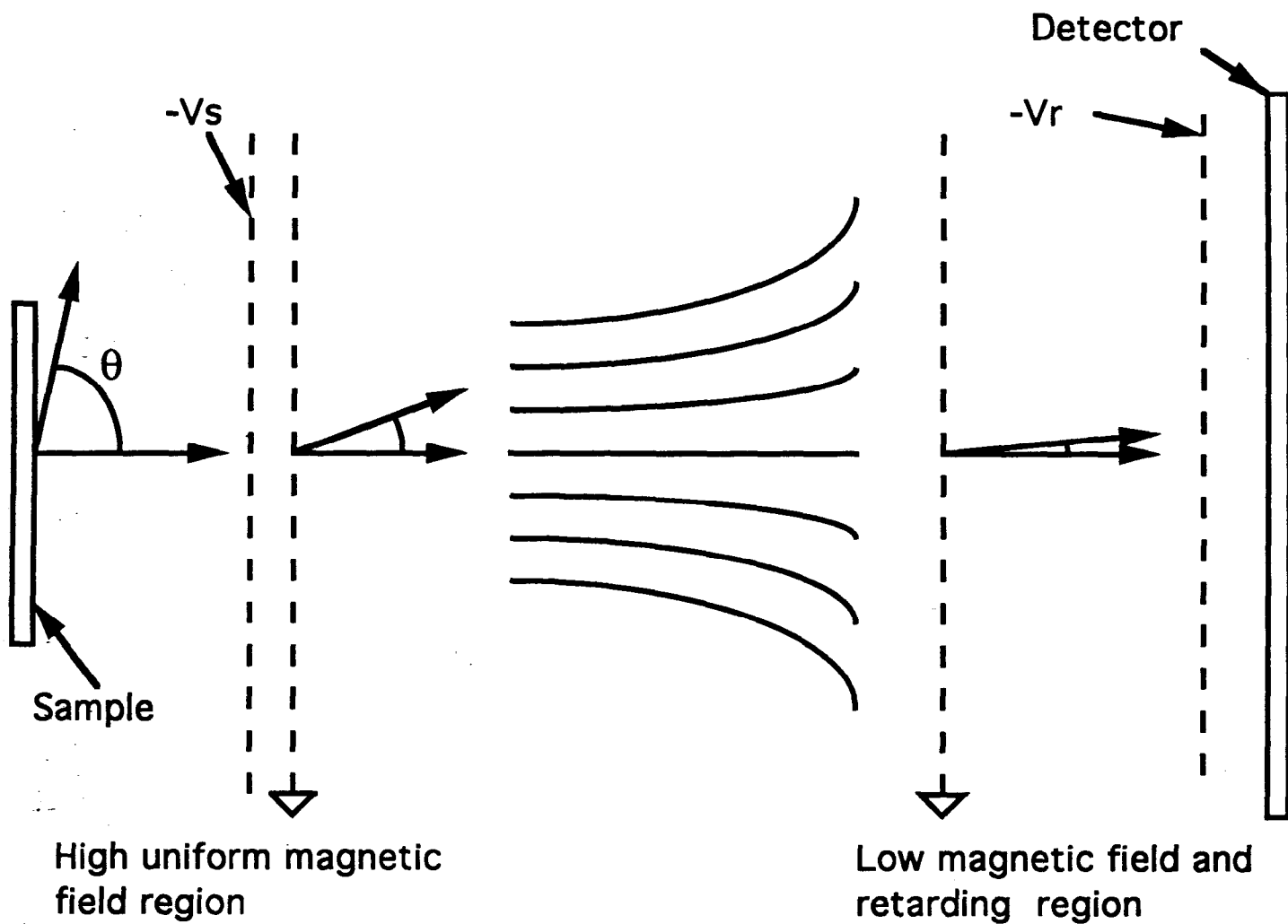


Fig. 5

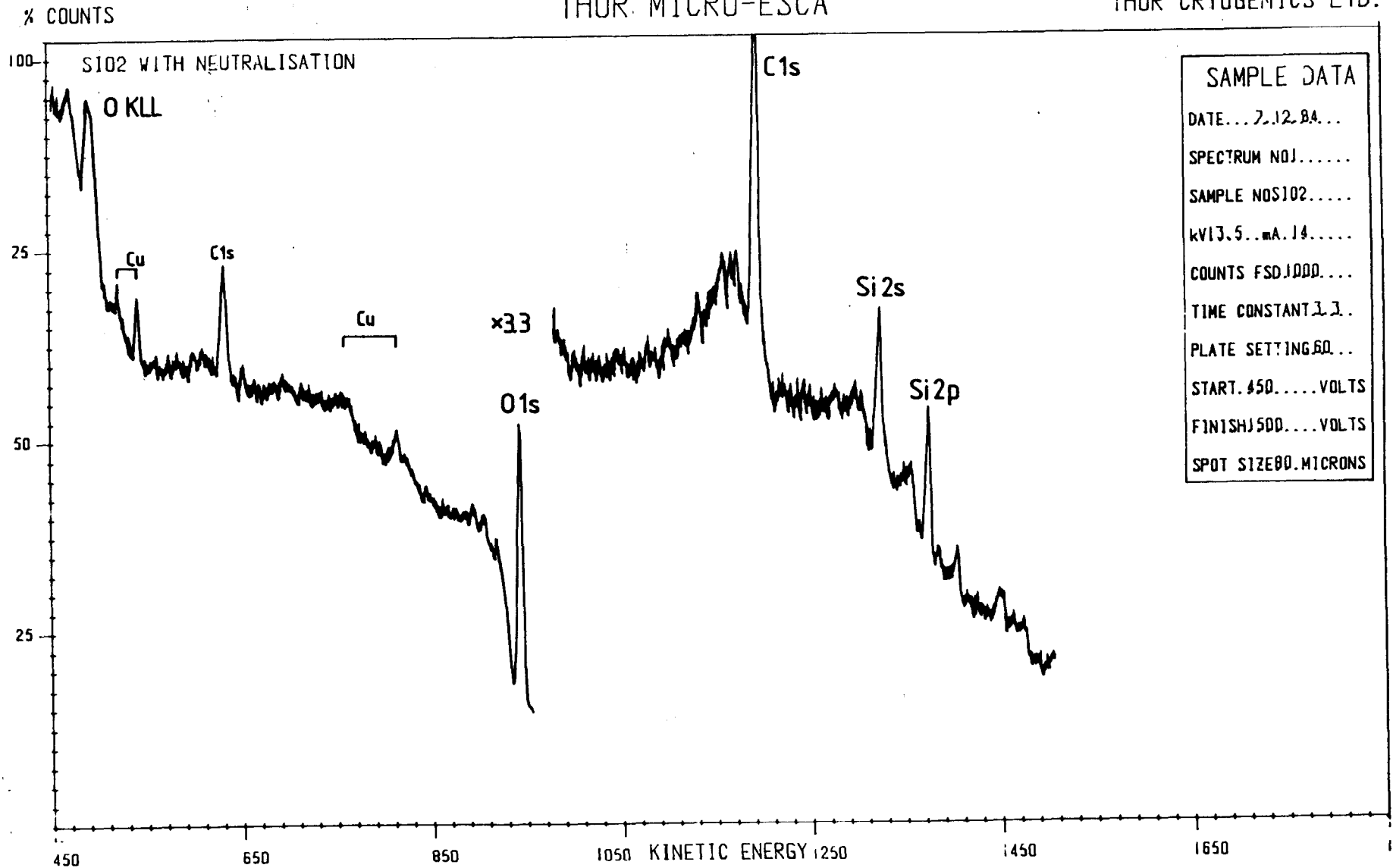


Fig. 6a

% COUNTS

THOR MICRO-ESCA

THOR CRYGGENICS LTD.

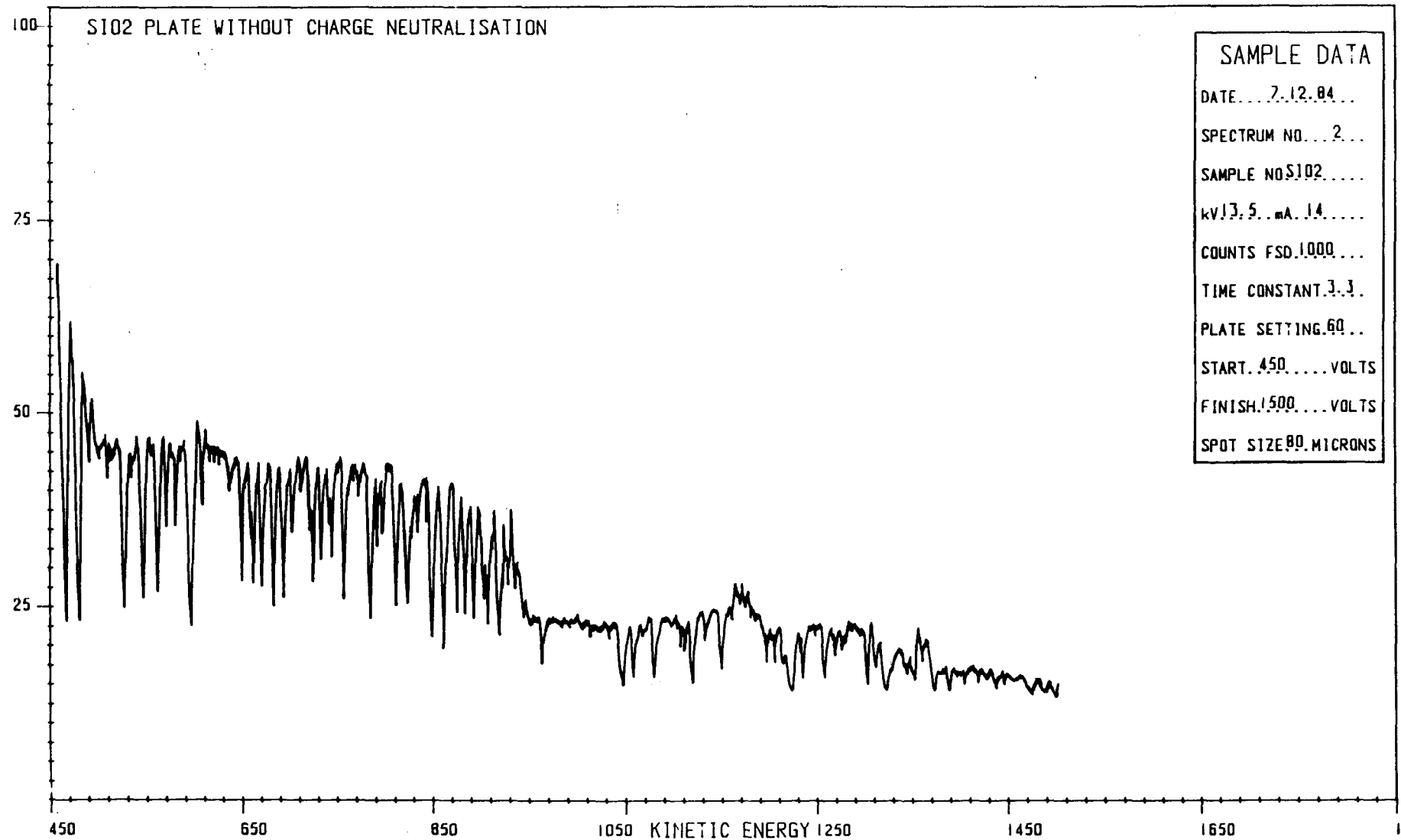


Fig. 6b



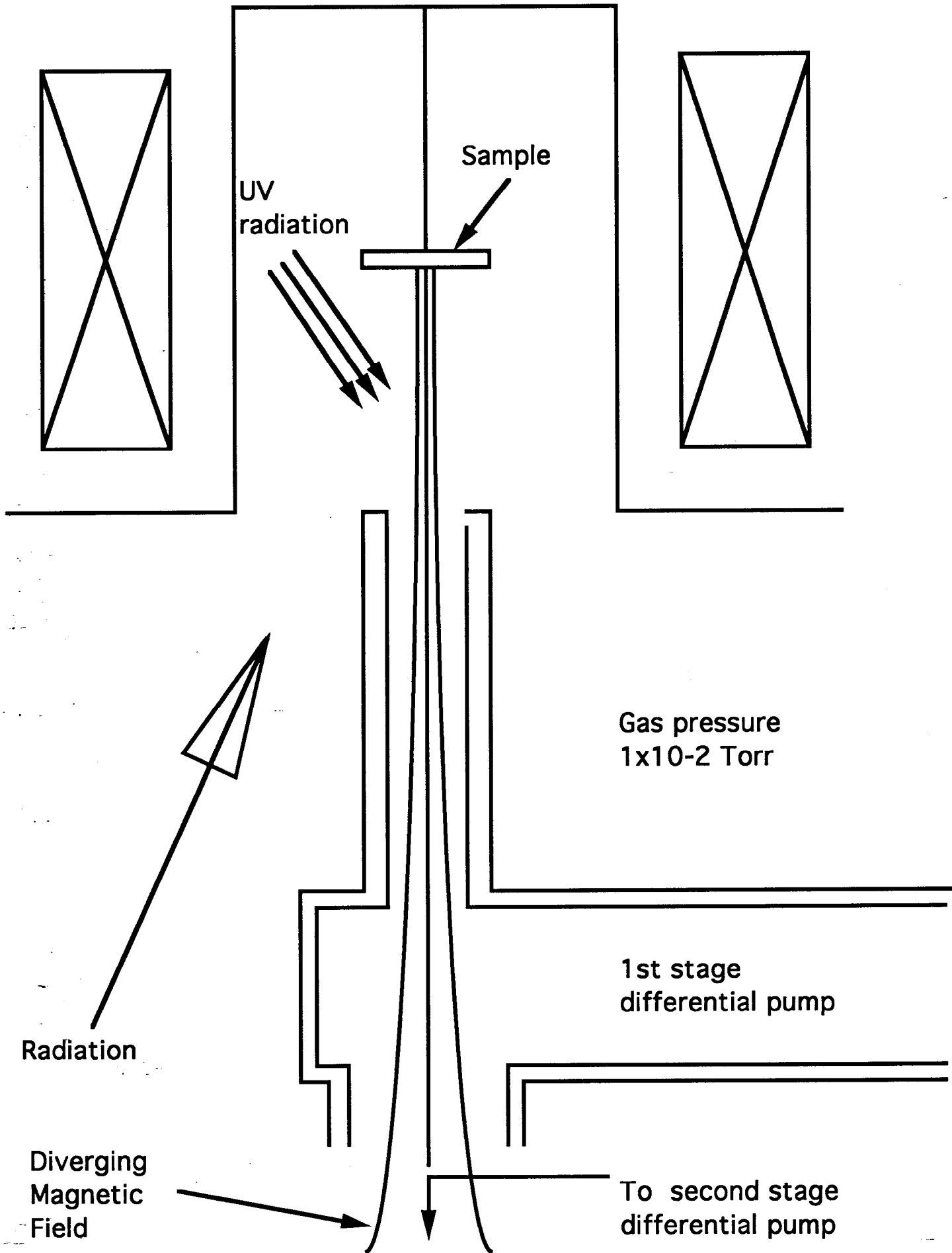


Fig. 7

Fig. 7



Fig. 8

% COUNTS

THOR MICRO-ESCA

THOR CRYOGENICS LTD

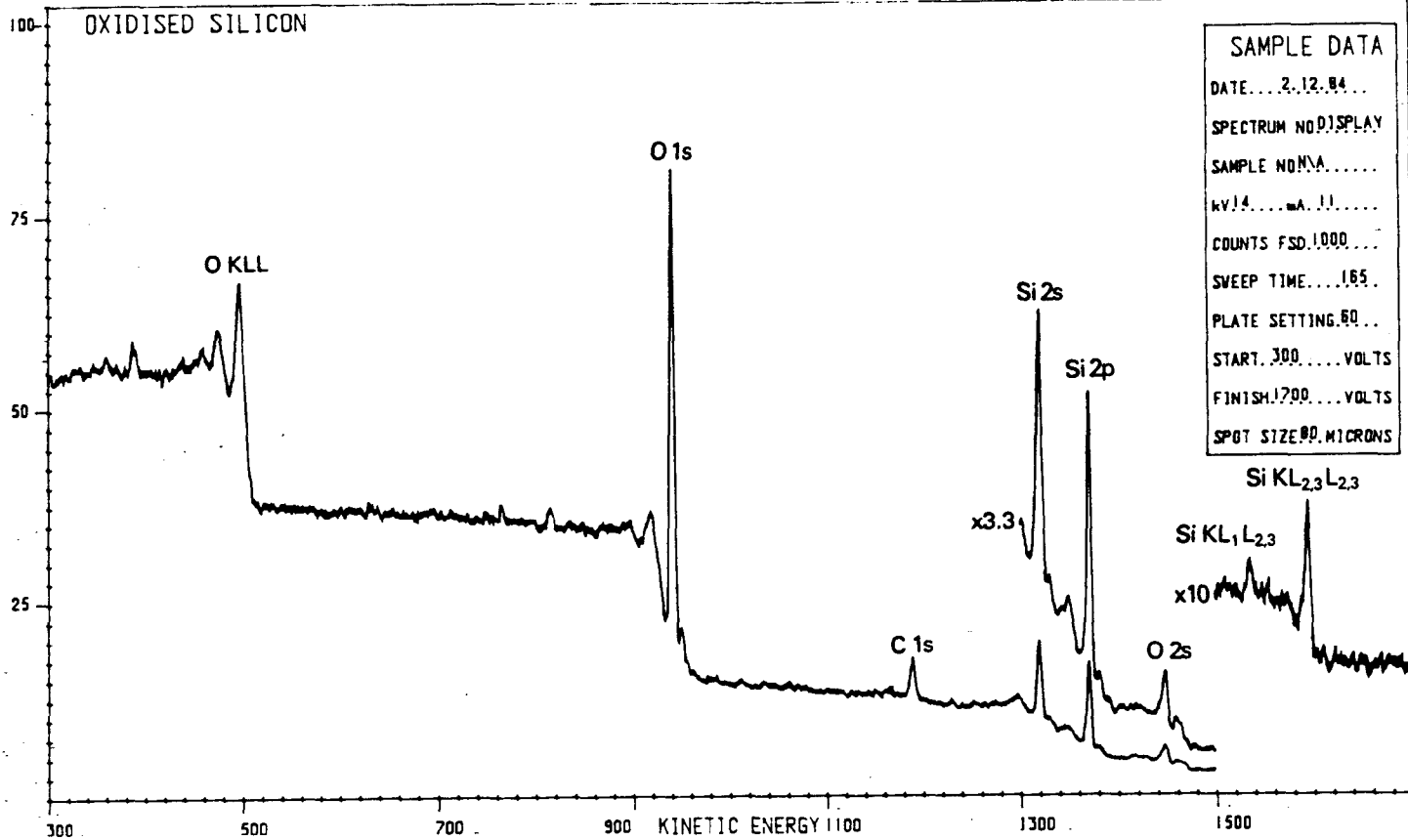


Fig. 9a

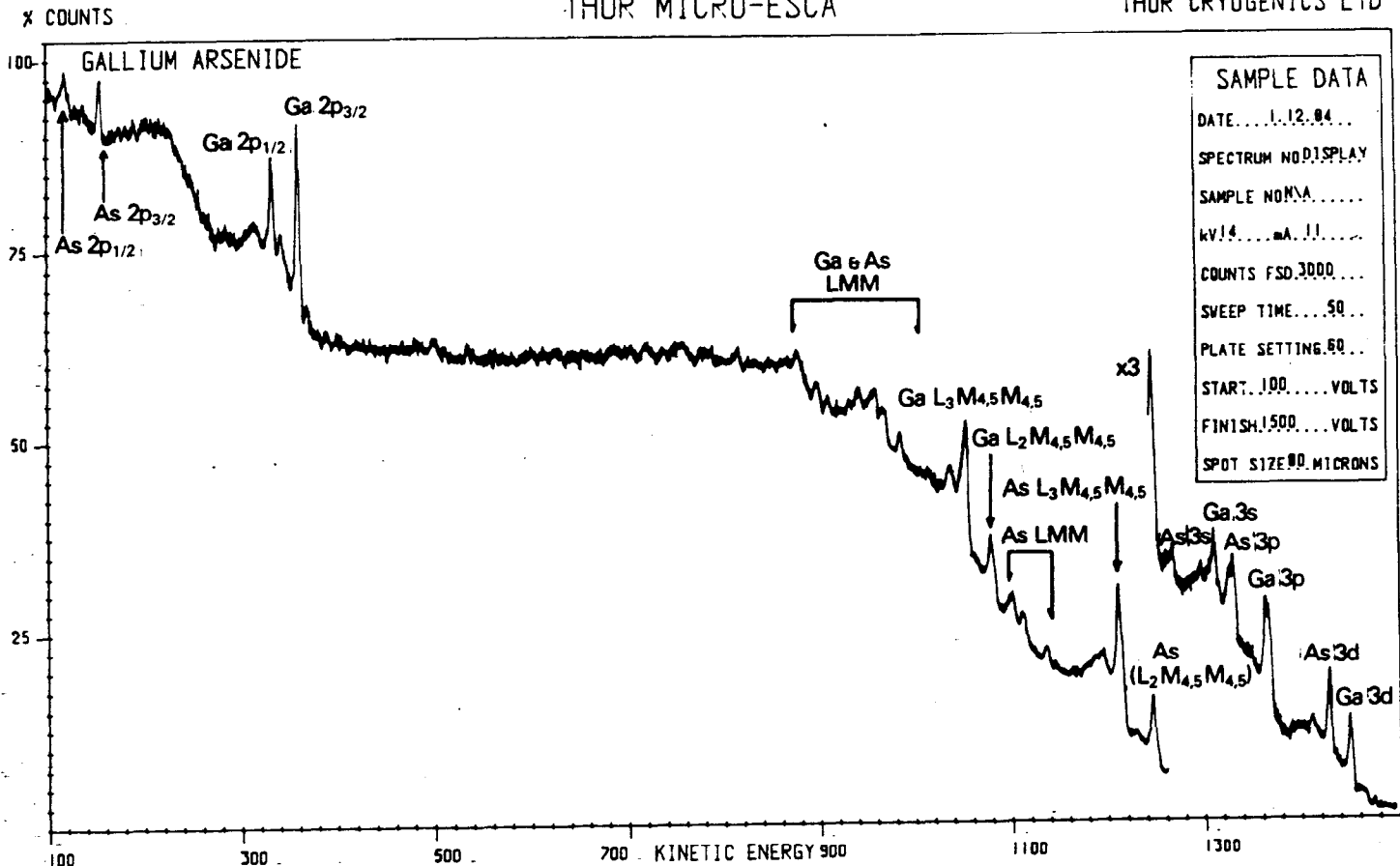


Fig. 9b

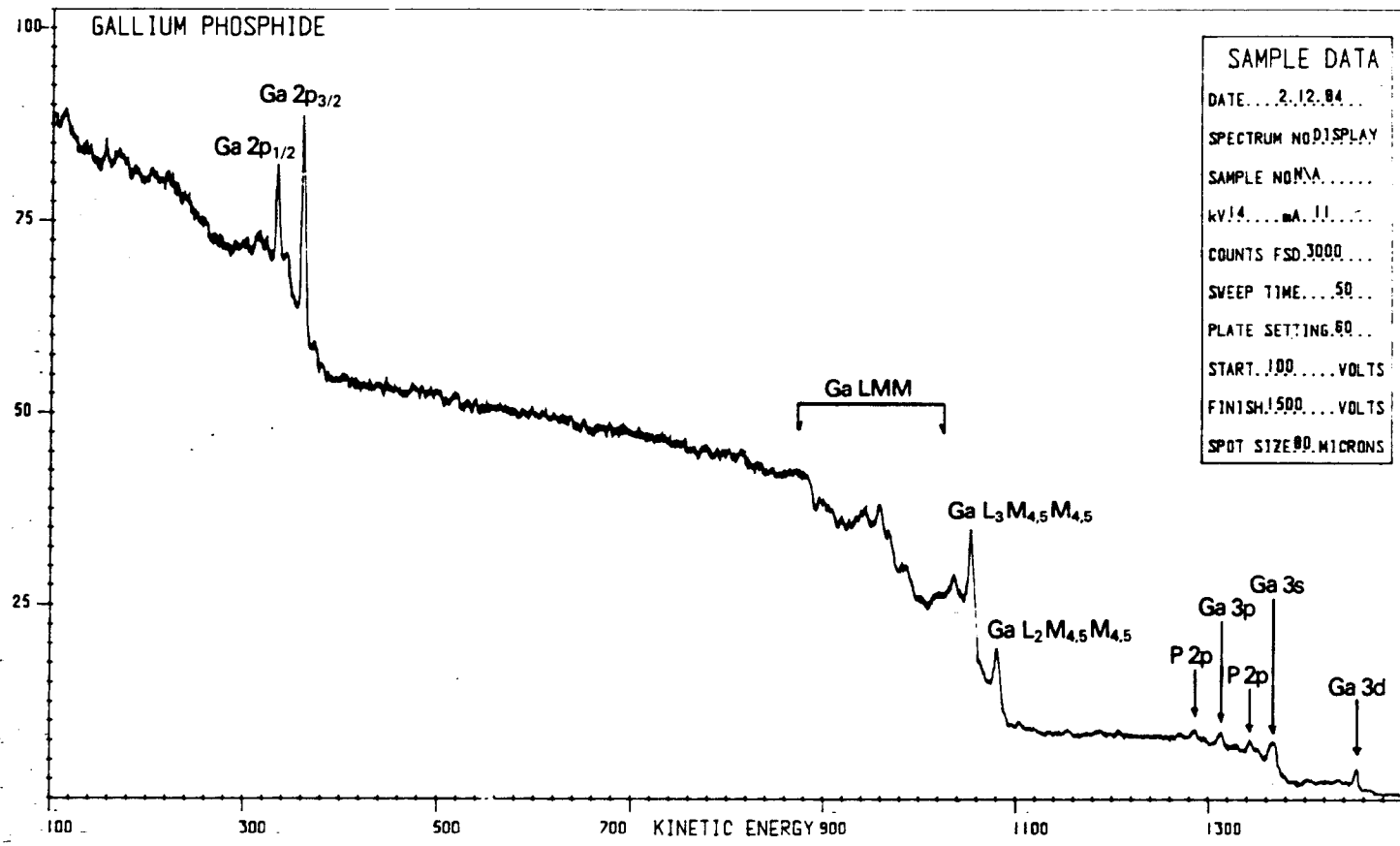


Fig. 9c

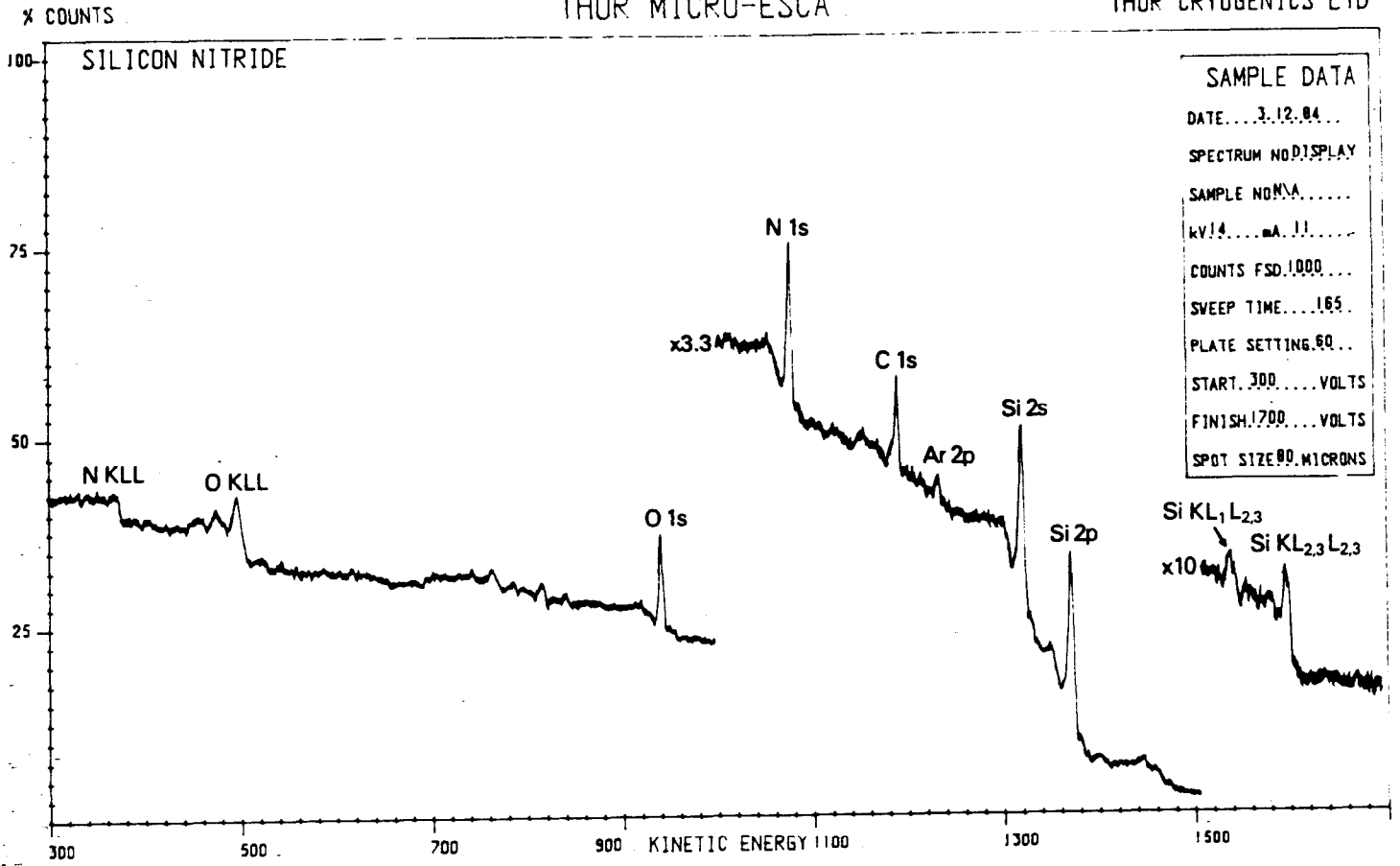


Fig. 9d

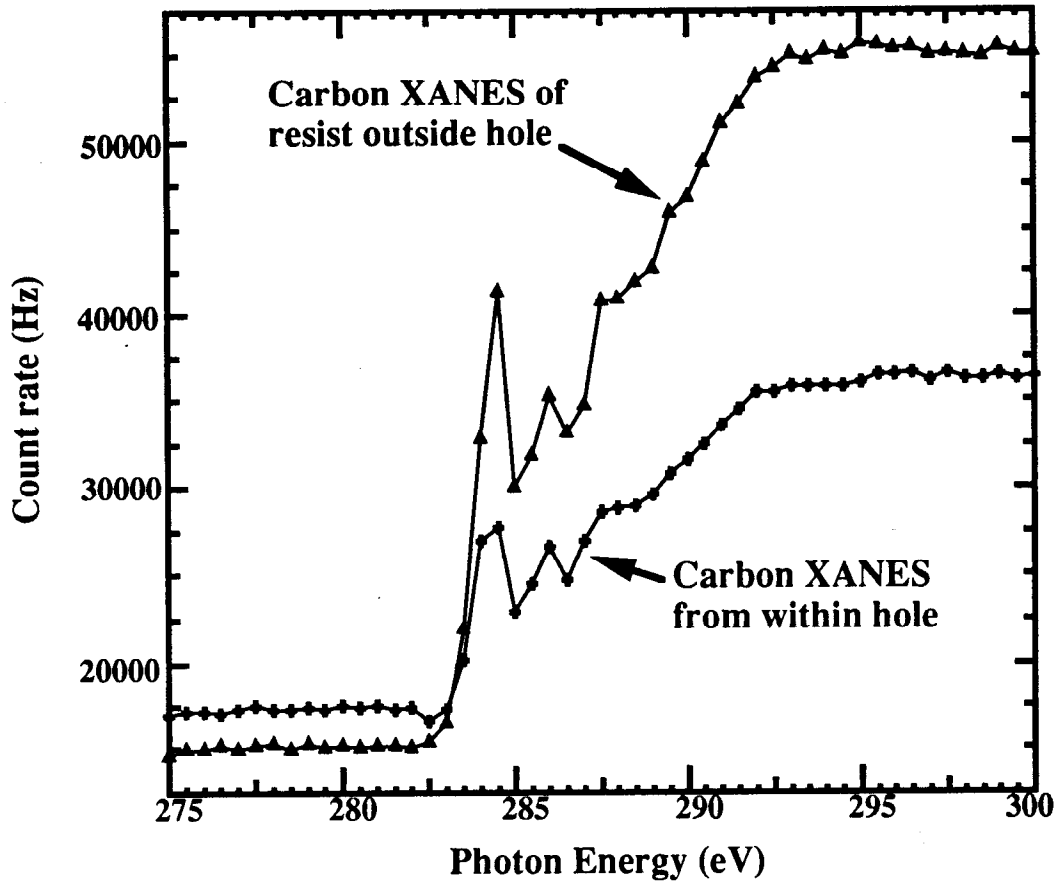


Fig. 10

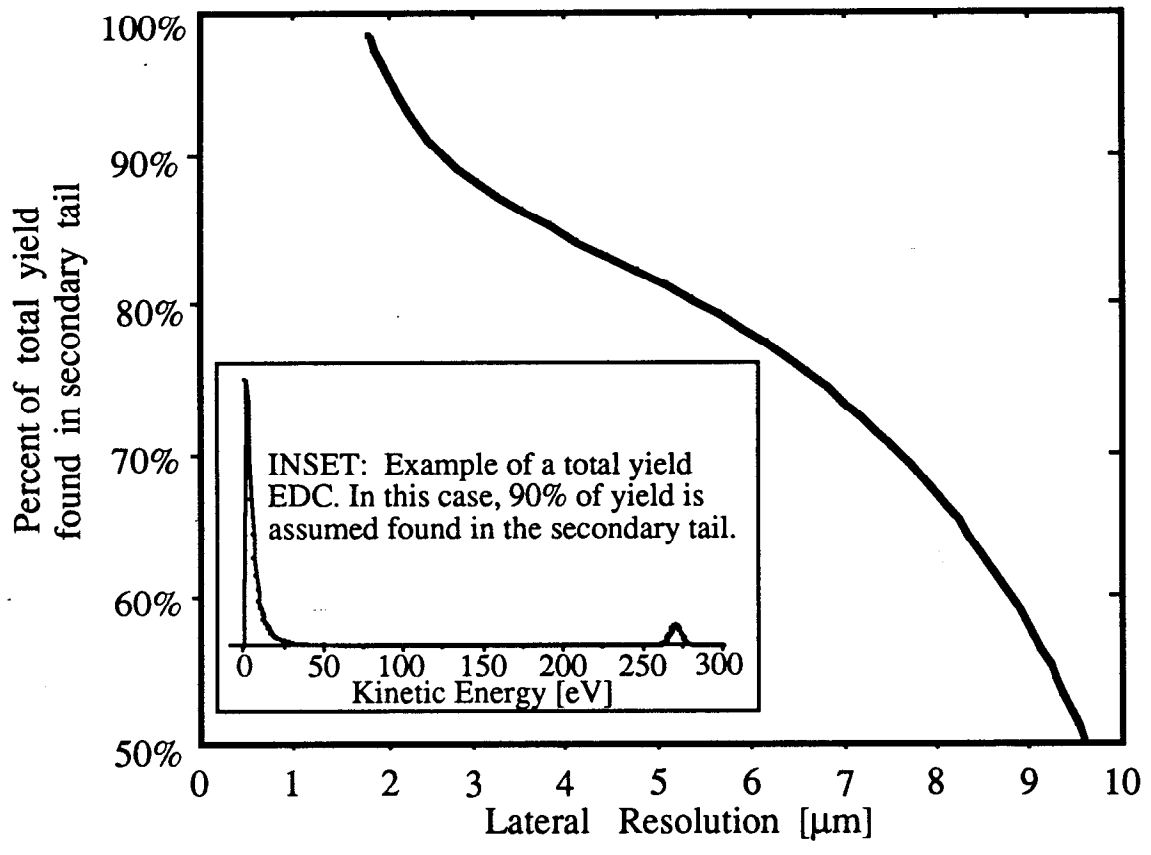


Fig. 11



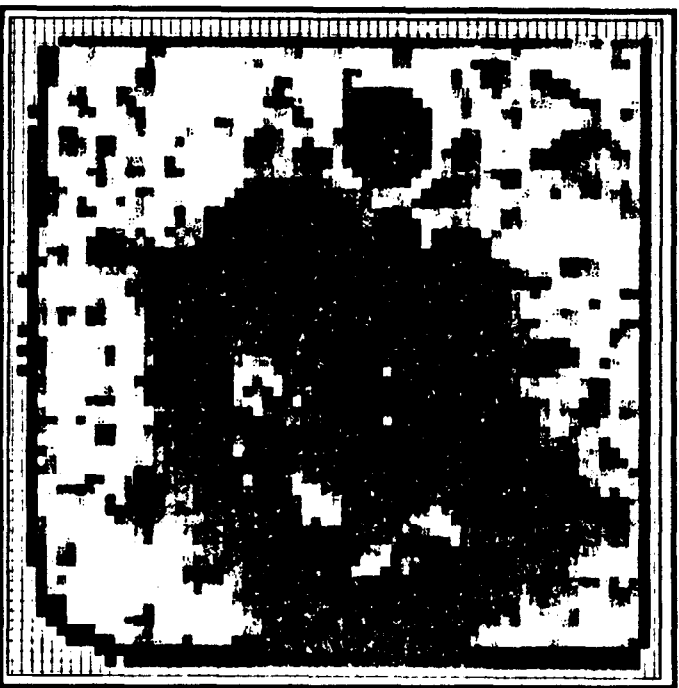


Fig. 12

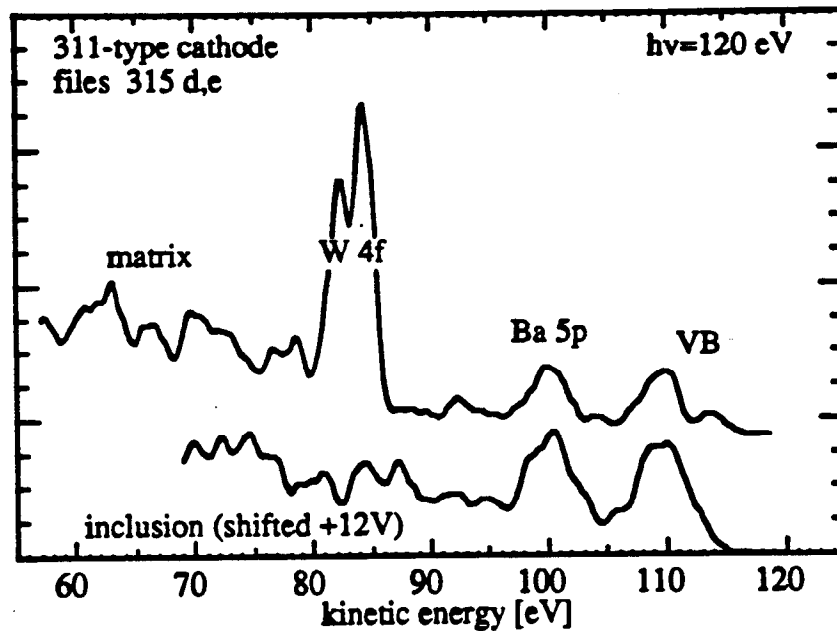


Fig .13

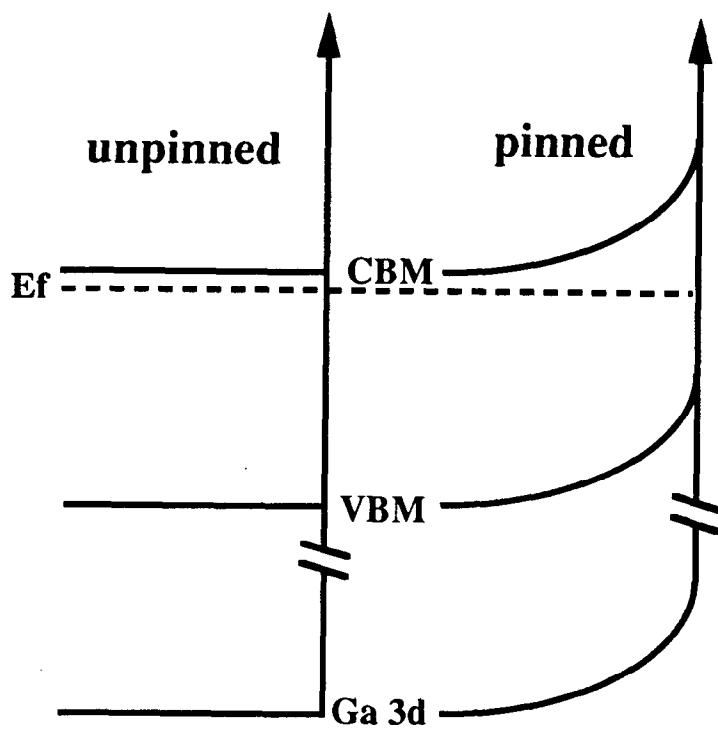


Fig. 14

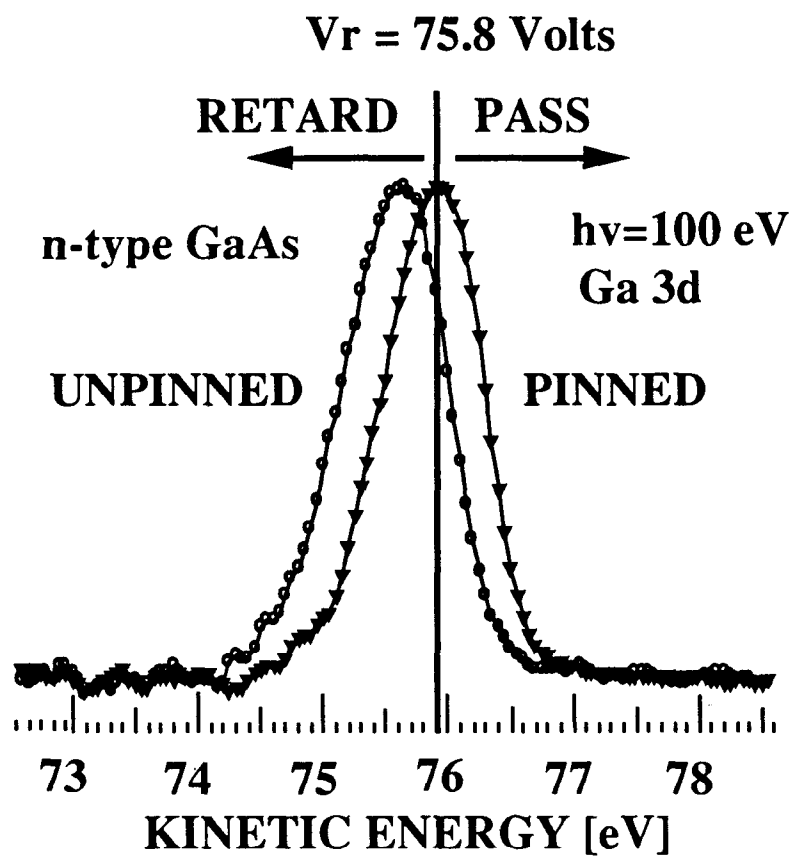


Fig. 15

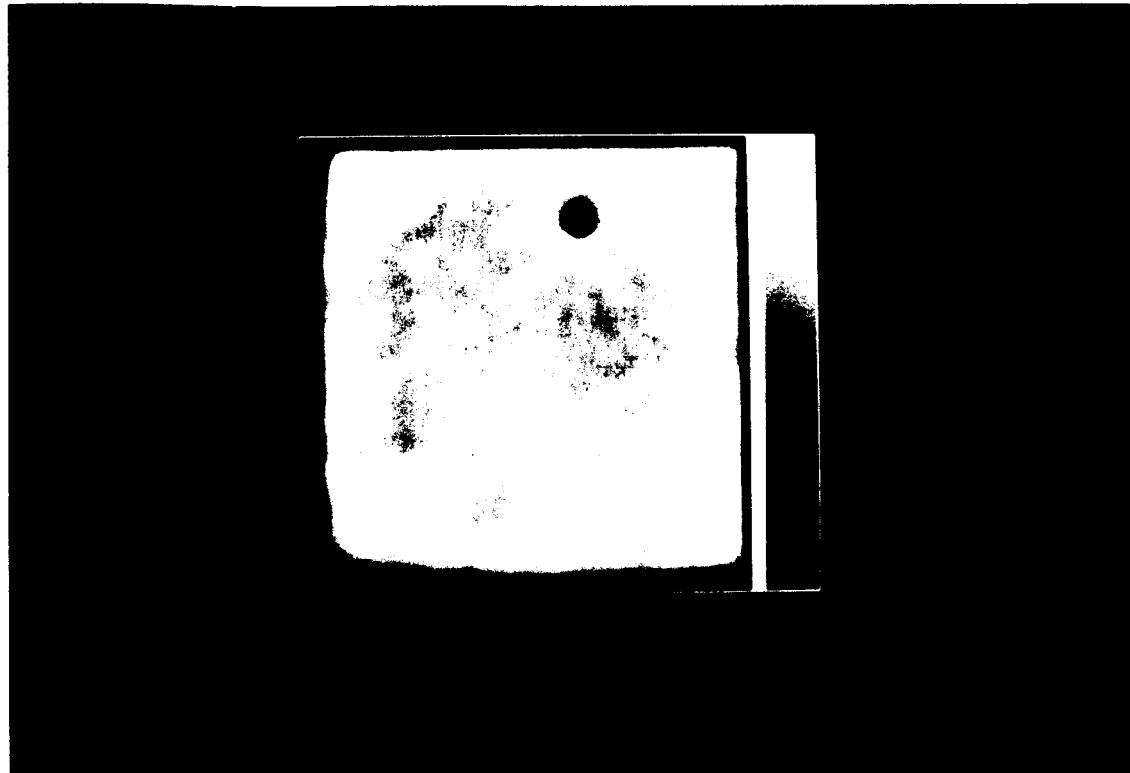


Fig. 16a



Fig. 16b

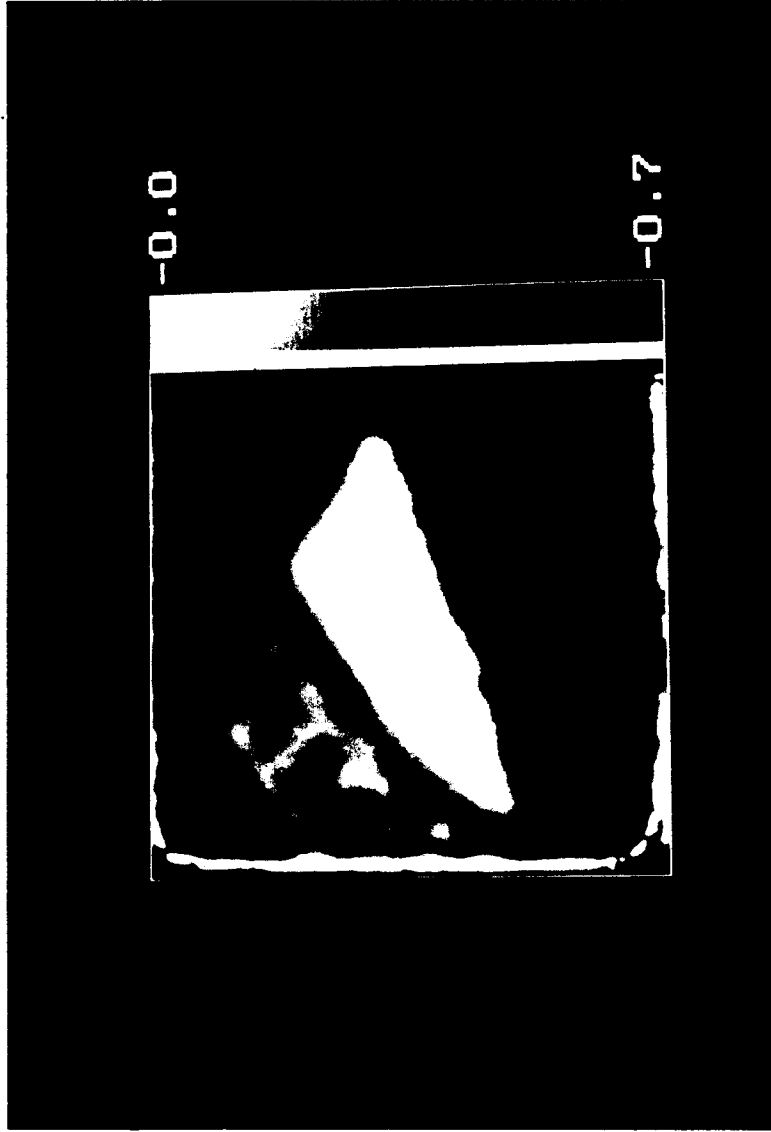


Fig. 16c

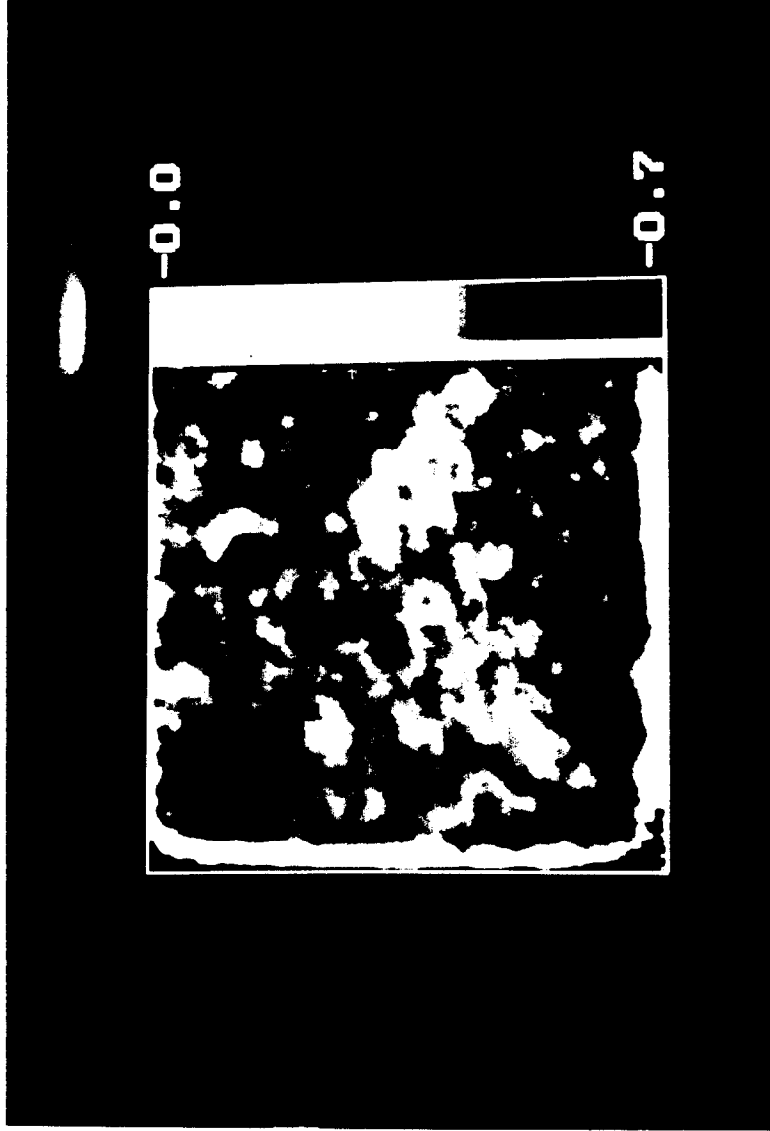


Fig. 16d